

Intrinsic heterogeneity of mossy cells mediates the differential crosstalk between the dorsal and ventral hippocampus

Minseok Jeong

DGIST

Jin-Hyeok Jang

DGIST

Seo-Jin Oh

DGIST

Young-Shik Choe

Korea Brain Research Institute

Jeongrak Park

DGIST

Junseop Lee

DGIST

Junwoo Park

DGIST

Yaebin Lee

DGIST

Sehyeon Hwang

DGIST

Jong Kim

DGIST <https://orcid.org/0000-0002-0257-0547>

Jusung Lee

DGIST, Daegu 42988,

Chang Man Ha

Korea Brain Research Institute

Yura Choi

Kyungpook National University School of Medicine

Sang Ryong Kim

School of Life Sciences, BK21 plus KNU Creative BioResearch Group, Brain Science and Engineering Institute, Kyungpook National University, Daegu 41566 <https://orcid.org/0000-0003-0299-1613>

Akinori Nishi

Kurume University School of Medicine <https://orcid.org/0000-0001-5056-5809>

Paul Greengard

The Rockefeller University,

Yong-Seok Oh (✉ ysoh2040@dgist.ac.kr)

DGIST <https://orcid.org/0000-0002-9039-2014>

Article

Keywords: Glutamatergic Mossy Cells, Distinct Axonal Projections, Comparative Transcriptional Profiling, Net Inhibitory Control, Dorsoventral Heterogeneity

Posted Date: October 26th, 2020

DOI: <https://doi.org/10.21203/rs.3.rs-92512/v1>

License:   This work is licensed under a Creative Commons Attribution 4.0 International License.

[Read Full License](#)

Abstract

Glutamatergic mossy cells (MCs) are responsible for the associational and commissural connectivity of the dentate gyrus. MCs are widely distributed along the dorsoventral axis, but potential heterogeneity within MCs is scarcely explored. Here, we showed that MCs consist of two subpopulations which differ in their neuronal properties and functions. We discovered that MCs, depending on their dorsoventral location, extend distinct axonal projections in the molecular layers. Comparative transcriptional profiling of dorsal and ventral MCs revealed different neurobiological characteristics in axon guidance and synapse assembly. Despite common activation by external stimuli, dorsal MCs, but not ventral MCs, provide net inhibitory control on granule cells across the longitudinal axis. Furthermore, dorsal MC inhibition, unlikely that of ventral MCs, increases behavioral anxiety and disables rapid contextual discrimination. Collectively, dorsoventral heterogeneity of MCs may provide a novel mechanism for functional differentiation as well as distinct association along the longitudinal extent of the hippocampus.

Introduction

The hippocampus plays critical roles in both cognitive and affective behaviors, and its dysfunctions are associated with a wide range of brain disorders ^{1,2}. The long curved structure of the hippocampus extends along the dorsoventral (DV) axis in rodents and the posterior/anterior axis in humans ³. Based on the traditional dichotomic view, the dorsal hippocampus has been associated predominantly with cognitive abilities, such as spatial and episodic memory, whereas the ventral side to a greater extent with anxiety-related behaviors ^{4,5}. DV differentiation of the hippocampus is causally linked to differential gene expression profiles in principal neurons as well as to neural connection within cortico-limbic structures ^{3,6}.

Mossy cells (MCs) are glutamatergic neurons in the dentate hilar region and are known to be vulnerable to neurotoxic insults such as ischemia, traumatic brain injury, and seizures ⁷. Loss or dysregulation of MCs results in abnormalities in dentate gyrus (DG)-mediated functions including spatial memory formation, pattern separation, and mood regulation ⁸⁻¹⁰. In the context of the DG circuitry, MCs receive dense excitatory inputs from nearby granule cells (GCs) through synaptic connections on their thorny excrescences ⁷. On the other hand, MCs extend long-range axonal projections to the inner molecular layer (IML), across the DV axis of the ipsilateral- and contralateral DG ^{11,12}. This unique projection pattern suggests the possibility that MCs may integrate local GC inputs and propagate their signals across the long axis of the DG ⁷. The neural circuits of MCs have the unique property of directly activating GCs ¹³, or indirectly inhibiting them via GABAergic interneurons ^{9,14,15}. Electron microscopy studies showed that the axonal arborizations of MCs in the IML of the DG make direct synaptic connections with proximal dendrites of GCs and also of GABAergic interneurons ^{12,16}. Genetic ablation of whole MCs results in transient hyperexcitability of GCs ⁸, whereas chemogenetic activation of MCs exert an excitatory effect on GCs ¹⁷, suggesting considerable inconsistency in the net effect of MCs on GCs. Considering the

functional heterogeneity of the hippocampus, it is plausible that MCs consist of multiple subpopulations with distinct properties and functions. However, the uniformity or heterogeneity of MCs along the DV axis remains unclear.

In this study, we found an intrinsic heterogeneity within the MC population. Our multidimensional analysis revealed that MCs are classified into at least two distinct subpopulations, dorsal MCs (dMCs) and ventral MCs (vMCs), which display significant differences in structural, molecular, and functional characteristics. This finding of drastic MC heterogeneity may contribute to a better understanding of the functional organization of the DG circuitry as well as of neural processing in the hippocampus.

Results

DV heterogeneity within MCs in their axonal projection pattern

Based on the histological distribution of the classical MC marker calretinin (CRT), MCs are known to project to the IML along the longitudinal axis of the DG¹⁸. However, CRT expression in MCs is limited to ventral DG (vDG), and thus does not represent the structural features of MCs in the dorsal DG (dDG). Therefore, the axonal projections pattern of dMCs remains uncharacterized, mainly due to the absence of a valid tracing marker for dMCs. Here, we compared the axonal projection patterns of dMCs and vMCs in an animal model by labeling them with selective EGFP- and tdTomato expression, respectively (Fig. 1a). Fluorescence protein expression in adeno-associated virus (AAV)-injected *Calcrl-Cre* mice was highly specific in MCs (dMCs: 95%±1.4, vMCs: 95%±1.7), but was undetectable in GCs and other interneurons such as parvalbumin-positive basket cells (PV + BCs) and hilar perforant path-associated cells (Supplementary Fig. 1). When visualized in horizontal sections along the DV axis (Fig. 1b), tdTomato-labeled axonal fibers of vMCs were found exclusively in the IML of the DG, which is consistent with the histological pattern of CRT expression¹⁸ (Fig. 1c). In contrast, EGFP-labeled axons of dMCs were found mainly in the IML and to a lesser extent in the middle molecular layer (MML) of the dDG (Fig. 1c, d). Strikingly, the relative density of dMC axons in these molecular layers was gradually shifted from IML to MML along the DV axis (Fig. 1c, d). Commissural axons from either dMCs or vMCs were found in the contralateral DG, and these layer-specific projections were highly consistent in the contralateral DG, despite the reduced density of axonal fibers as compared with that in the ipsilateral DG (Fig. 1e, f). Furthermore, CRT expression fully overlapped with tdTomato-labeled vMCs in the hilus as well as their axons in the IML, but not with EGFP-labeled dMCs or their axons (Supplementary Fig. 2), confirming that EGFP-labeled axons along the DV axis originate from dMCs, but not from vMCs.

For holistic visualization of axonal projections of MCs in an intact hippocampus, we took advantage of the CLARITY technique. Our three-dimensional rendering images showed that dMCs and vMCs project to the bilateral DG through the dorsal and ventral hippocampal commissure, respectively (Supplementary Movie 1). Consistent with confocal images of hippocampal sections, a holistic view of MC projections

displayed clear layer specificity along the DV axis of the DG (Fig. 1g). Furthermore, we noticed that longitudinal axons from dMCs and vMCs cover roughly up to 80% of the entire DG (Fig. 1g), highlighting the structural nature of MCs in the DG network. Taken together, dMCs and vMCs, display distinct projection patterns along the longitudinal axis of the DG (Fig. 1h).

Spatial distribution and cell quantities of two distinct MC subpopulations

The hippocampus is organized into multiple functional domains, which often exhibit sharply demarcated borders or linear gradient patterns along the DV axis³. Thus, we examined the spatial distribution of each MC subpopulation along the DV axis by double staining with GluR2/3 as a pan-MC marker and CRT as a vMC marker (Fig. 2a, b). dMCs (GluR2/3+|CRT-) were found in the dorsal one-third of the whole DG. They were well-segregated from vMCs (GluR2/3+|CRT+), with a narrow borderline (bregma: -2.1 mm, D-V) where the two populations intermingled (Fig. 2c). As a rough estimate, a total of around $6,122 \pm 157$ MCs (GluR2/3+) were counted per hippocampus (2487 ± 143 dMCs and 3635 ± 119 vMCs), indicating the presence of fewer dMCs than vMCs (Fig. 2d). Our proportion analysis showed that the dMC subpopulation was smaller than the vMC one (Fig. 2e). Taken together, these results suggest that MCs are divided into at least two subpopulations, which are spatially segregated with a narrow border line in-between.

Transcriptional heterogeneity of MCs along the DV axis of the DG

To investigate the molecular heterogeneity between dMCs and vMCs, we utilized the translating ribosome affinity purification (TRAP) method in combination with RNA-seq analysis. The Calcr1-Cre driver is highly cell-type specific in AAV-injected adult animals, but not in double transgenic animals with floxed (ribosomal subunit L10a) EGFPL10a, most likely due to transient CA3 expression from the Cre-cassette during the earlier development stage. Alternatively, we adopted the Drd2-Cre driver to ensure higher EGFPL10a labeling specificity of the MC transcriptome (Drd2-Cre;floxed EGFPL10a) (Fig. 3a)¹⁰. In order to differentiate the transcriptome of each MC subpopulation, we divided the hippocampus into the dorsal one-third and the remaining ventral part (Fig. 3b), based on their distribution pattern along the DV axis (Fig. 2). Our quantitative PCR analysis of each fraction verified that *Gria3*, encoding the pan-MC marker GluR3, was expressed in both dMCs and vMCs, whereas *Calb2*, encoding the vMC marker CRT, was expressed at a much higher level in vMCs (Fig. 3c), consistent with Allen Brain Atlas (ABA) *in situ* hybridization (ISH) data (Supplementary Fig. 3a). Parallel RNA-seq analysis of both fractions identified differentially expressed genes (DEGs) in each MC subpopulation (Supplementary Table 1). A total of 1442 genes were highly enriched in the dMC fraction. Conversely, 1337 other genes were enriched in vMCs, indicating a significant difference between dMC and vMC gene expression patterns (Fig. 3d, e). According to our transcriptomic profile of the MC subpopulations, *Cyp26b1* expression is higher in dMCs, whereas *Adcyap1* expression is higher in vMCs, which was cross-validated with the ABA ISH data (Supplementary Fig. 3b).

To categorize differential functional characteristics for each MC subpopulation based on transcriptomic features, we reviewed the annotations of all dMC and vMC DEGs in Mouse Genome Informatics database. Functional enrichment analysis revealed distinct biological processes and Kyoto Encyclopedia of Genes and Genomes (KEGG) pathway associated with each MC subpopulation. Notably, dMCs were enriched in multiple genes associated with axonal guidance, cell adhesion, synaptic assembly, and synaptic transmission (Fig. 3f, g). In contrast, vMCs expressed higher levels of genes associated with metabolic and proteasomal processes, and synaptic recycling (Fig. 3f, g). We further reclassified these gene families into the following functional groups: neuronal connectivity (axon guidance, cell adhesion, and synapse assembly), synaptic transmission (neuroactive ligand-receptor and ion channels), neuronal metabolism (glucose and fatty acid metabolism), and cellular processes (oxidative stress, proteasome, and exocytosis) (Fig. 3h, i). To single out individual genes in these functional categories, we ranked the top 20 genes based on absolute fold enrichment between MC subpopulations (Fig. 3j, k; Supplementary Fig. 3c-e; Supplementary Table 2). Notably, distinct subsets of axon guidance and cell adhesion molecules genes, including Eph-ephrin and plexin-semaphorin family genes, were found to be differentially expressed in dMCs and vMCs (Fig. 3j; Supplementary Fig. 3c). Altogether, our genomic approach revealed molecular heterogeneity within MCs, which represents the distinct neurobiological characteristic of each MC subpopulation.

Net inhibitory control of dentate GCs by dMCs but not by vMCs

To examine whether external stimuli activate each MC subpopulation differentially, we exposed the animals to contextual fear conditioning (CFC) (Fig. 4a). The acute induction of c-Fos, a neural excitation marker was utilized to monitor the activity change of MCs along the DV axis. Our results suggest that dMCs and vMCs are both likely activated by contextual stimuli (Fig. 4b, c), regardless of their DV location. Next, we investigated how each MC subpopulation influences GC activity along the longitudinal axis of the DG. Floxed control and Gi-coupled designer receptor exclusively activated by designer drugs (Gi-DREADD) AAVs were injected into either the dorsal (D-control and D-hM4Di) or ventral (V-control and V-hM4Di) hilus for chemogenetic inhibition of each MC subpopulation (Fig. 4d, e). Our previous electrophysiological recordings have shown strong inhibitory control of MC activity with the clozapine-N-oxide (CNO)/Gi-DREADD system¹⁰. After CNO injection, the animals underwent CFC, and GC activation was assessed based on c-Fos immunoreactivity in a series of DV sections (Fig. 4f). Interestingly, acute inhibition of dMCs facilitates CFC-induced GCs activation throughout the DV extent of the DG, which was not reproduced by equivalent control of vMCs (Fig. 4g, i), indicating the selective role of dMCs in GC inhibition along the DV axis.

GCs receive main excitatory inputs from the entorhinal cortex, but their excitations are controlled by tight perisomatic inhibition from GABAergic PV + BCs, which plays a key role in several higher functions, such as feedforward, feedback inhibition, and pattern separation^{19,20}. Therefore, we postulated that longitudinal projections of dMCs provide stimulatory inputs onto PV + BCs, which suppress the excitability of GCs across the DV axis of the DG. To test this possibility, we analyzed c-Fos expression in PV + BCs in animals with dMC inhibition. Notably, acute inhibition of dMCs markedly reduced c-Fos

immunoreactivity of PV + BCs across the DV axis of the DG, but more strongly in the vDG than in the dDG (Fig. 4j, l). These results suggest that dMCs, upon contextual stimulus, carry out net inhibitory control of GCs, indirectly through long-range activation of PV + BCs.

Selective involvement of dMCs in anxiety regulation and pattern separation

The dDG and vDG have been differentially implicated in cognitive and affective behaviors⁵. Our observation regarding the DV regulation of GC excitability by dMCs, led us to examine the putative behavioral outcome of dMC inhibition especially in term of anxiety and contextual memory. First, we examined anxiety-like behaviors after selective inhibition of either dMCs or vMCs (Fig. 5a, b). Acute chemogenetic inhibition of dMCs, but not of vMCs, significantly reduced total duration in the open arms of the elevated plus maze (Fig. 5c) without altering general locomotor activity. Consistently, our open field test results showed that exploration activity in the center zone was drastically reduced in animals with chemogenetic inhibition of dMCs, but not of vMCs (Fig. 5d), suggesting selective involvement of dMCs in anxiety-like behaviors.

Next, we examined the selective implication of MC subpopulations in contextual fear memory. We silenced each MC subpopulation prior to fear exposure and tested fear memory retrieval in the same context (Supplementary Fig. 4a). Strikingly, neither dMC- nor vMC- inhibition influenced freezing behavior in the given context (Supplementary Fig. 4b), suggesting that MCs are not involved in the encoding of fear memory. We further investigated the putative role of MCs in discriminating between different contexts. Animals were conditioned in context A with foot shock for 3 days (Supplementary Fig. 5a), which was followed by a generalization period with alternative exposure to context A and B without foot shock for 2 days (Supplementary Fig. 5b). We then performed contextual discrimination training (fear context A, safe context B) with selective inhibition of each MC subpopulation daily for 12 days (Fig. 5e, f). All animals displayed strong freezing behaviors in context A after fear conditioning (Supplementary Fig. 5a). During fear generalization, these animals also developed freezing behavior in context B, an unconditioned context. We observed no visible difference in freezing behaviors in each context between the comparison groups (Supplementary Fig. 5b). Thereafter, animals were administrated CNO prior to daily contextual discrimination training (Fig. 5f). Dorsal and ventral control groups began to distinguish contexts A and B from block 2 (Fig. 5g, h). Pattern separation was deferred by selective inhibition of either MC subpopulation (Fig. 5g, h). Notably, dMC- and vMC-inhibition delayed contextual discrimination by additional 2 blocks (4 days) and 1 block (2 days), respectively, suggesting a more significant role of dMCs in this rapid pattern separation (Fig. 5g, h). Indeed, pattern separation at blocks 2 and 3 was normal in the vMC inhibition group, but was significantly impaired by dMC inhibition, despite complete pattern separation in both groups at block 5 (Fig. 5i, j). Collectively, these results suggest functional heterogeneity within MCs, especially in affective and cognitive behaviors.

Discussion

The hippocampus is functionally differentiated along the DV axis, and this differentiation has been ascribed to differences in afferent/efferent connectivity and gene expression in principal cell types (CA1, CA3, and DG) ^{3,6}. In this study, we found that MCs, depending on their DV location, differ significantly in axonal projection patterns. We clearly visualized distinct layer-specific projections of dMCs and vMCs along the DV axis. Unlike vMCs projecting to the IML only, dMCs innervate either the IML or the MML depending on the DV position. Topographic projections in the hippocampus are governed by a complex interplay among axon guidance and cell adhesion molecules ²¹. It is notable that dMCs express higher levels of multiple Eph receptor subtype genes (*Epha4*, *Epha5*, *Epha7*, *Ephb1*) and *Sema5a*, *PlexnA4*, and *Robo3*, which play a key role in axon guidance. In contrast, vMCs express multiple Eph ligand genes (*Efna1* and *Efnb2*). Interestingly, entorhinal axons expressing *Epha5* are repelled from the Eph ligand-expressing IML of the DG ²². In addition, retinal ganglion cell axons expressing *ephb1* avoid the midline at the *efnb2*-expressing optic chiasm, thereby establishing a partial decussation ²³. Topographically organized projections of MCs to the molecular layers are attributable to differential expression of axon guidance molecules in each MC subpopulation, as well as to the DV gradient of their cognate ligand/receptors in the molecular layers.

There is considerable controversy regarding whether glutamatergic MCs excite or inhibit GCs ^{8,9,13,24}. Here, we found that MCs, depending on their DV location, exert different net effects on GC excitability. Our data showed that the inhibition of dMCs, but not vMCs, resulted in GC hyperexcitability across the longitudinal axis. This is caused by the suppression of excitatory dMC input to widespread PV + BCs, followed by the loss of perisomatic inhibition onto local GCs. PV + BC dendrites extend across all molecular layers and receive the majority of excitatory synaptic inputs from the entorhinal cortex and MCs. It is of note that dendritic segments of PV + BCs display non-uniform cable properties, with a 10-fold higher membrane resistance at distal dendrites (MML and OML) than at proximal dendrites (IML), which likely accounts for the stronger synaptic inputs at distal dendrites ²⁵. Presumably, topological projections to the MML favor dMCs to provide strong excitatory inputs to PV + BCs along the DV axis, in comparison to vMCs projecting only to the IML. Furthermore, synaptic specificity and strength are largely determined by adhesion and synaptic assembly molecules expressed in pre- and post-synaptic neurons ²⁶. It is intriguing to speculate that differential gene expression may underlie the synaptic specificity of dMCs and vMCs onto their post-synaptic target cells. Interestingly, dMCs are enriched in a subset of synaptic regulators, including *Epha7* and *Nrg3*, that are known to promote the excitatory synaptogenesis onto PV + BCs in the hippocampus ^{27,28}. Indeed, a recent study using electron microscopy showed that dMCs innervate PV + BC dendrites to a much higher extent than vMCs do ¹⁷. It also reported that vMCs have a net excitatory effect on GCs in a novel environment, although we could not observe similar effect in our CFC paradigm. Altogether, these observations suggest that distinct projections from dMCs and vMCs may regulate GC excitability via a differential excitatory/inhibitory balance in given conditions. Future studies to determine relative dominance in post-synaptic targets of each MC subpopulation by using electrophysiology with layer-specific manipulation of MC axons and further quantitative electron microscopy with axonal labeling of each subpopulation are warranted.

The DG first receives multiple sensory inputs from the entorhinal cortex, which integrates diverse contextual and emotional information, as a gateway to the trisynaptic circuit²⁹. Moreover, the dDG and vDG have been differentially associated with contextual representation and anxiety control, respectively^{5, 30}. In this regard, it is striking that dMC inhibition results in elevated anxiety-like behaviors, which seems contradictory to DV differentiation of DG functions, in that anxiety control has been associated with the ventral portion of the hippocampus. However, we showed that inhibition of dMCs results in ventral GC hyperexcitability, which has been causally linked to elevation of anxiety responses³⁰. Consistent with this, direct manipulations of PV + BC activity in the DG altered anxiety-like behaviors^{31, 32}. Therefore, dMCs may regulate anxiety-like behaviors with longitudinal control of the DG network, primarily through PV + BCs. It is intriguing to speculate that dMC may integrate contextual information from the dDG and convey it to the vDG for driving contextual memory associated with emotional valence.

Here, we also found that MC inhibition had no effect on memory encoding, but significantly delayed contextual discrimination, which consistent with the established roles of the DG in contextual processing^{33, 34}. The sparse activation pattern of GCs is required for context-specific representation, which is essential for pattern separation between similar contexts²⁹. Adequate inhibition of extra neural ensembles beyond the extant engram pattern is critical for discriminating input patterns in the DG. Therefore, it is important that dMCs provide indirect inhibition onto GCs through PV + BCs. In fact, dysregulation in the high-frequency firing of PV + BCs impairs spatial pattern separation in the DG³¹. Supporting this idea, computational modeling suggests that inhibition of MC-to-BC connections resulted in the recruitment of significantly more GCs in response to simulated entorhinal input. Interestingly, direct excitatory MC-to-GC connections have insignificant effects on the sparseness of GC activation and on pattern separation efficacy³⁵. Thereby, dysregulation of the GC excitation pattern with dMCs inhibition is responsible for impaired pattern separation, possibly with increased uncorrelated noise in the GC ensemble. Meanwhile, vMCs were reported to convey predominantly excitatory inputs to dorsal GCs¹⁷, which may account for why vMC inhibition has rather marginal effect on rapid pattern separation. Collectively, the differential dominance between direct (MC-to-GC) and indirect (MC-to-BC) pathways may underlie the distinct function of each MC subpopulation during memory processing. To further explore how each MC subpopulation influences the GC ensemble pattern, future work may require animal models in which the GC ensemble is traceable in real-time in the given contexts, while under simultaneous manipulation of each MC subpopulation.

Conflicting with a classical dichotomic view of the hippocampal functions along the DV axis, there is growing evidence suggesting that contextual processing depends on not only the dorsal but also the ventral portions of the hippocampus. Lesioning or pharmacological manipulations of the ventral hippocampus often impair contextual processing that was traditionally ascribe to the dorsal one^{36, 37}. Furthermore, dorsal and ventral young GCs contribute to contextual-dependent memory³⁸. In addition, the vDG, but not the dDG, is critical for odor discrimination³⁹, supporting differential contextual representation in the dDG and the vDG. MCs receive dense excitatory inputs from nearby GCs and

propagate their excitatory signals across the long axis of the DG circuitry. This longitudinal projection of MCs may mediate functional crosstalk between the dDG and vDG, and thereby enable functional integration throughout whole DG networks along the DV axis. Our findings highlight the within-cell-type heterogeneity of MCs, as dMCs and vMCs significantly differ in their net effects on GC excitability (Supplementary Fig. 6). This dorsoventral heterogeneity of MCs may represent a significant difference in MC-mediated crosstalk between the dDG and vDG. Our findings may provide a novel mechanism underlying the dorsoventral differentiation of the DG circuitry, as well as the functional association of the entire DG network to control cognitive and affective behaviors.

Materials And Methods

Animals

The following transgenic (TG) lines were imported from the Jackson (JAX) laboratory: Calcr1-Cre TG (JAX stock, #023014) and Eef1a-LSL-EGFPL10 TG (JAX stock, #030305). Another TG line, Drd2-Cre TG (GENSAT, Clone #ER44), was imported from GENSAT. All TG mice were bred with C57BL/J mice (JAX) to obtain hemizygotes. Drd2-Cre TG (hemizygote) mice were cross-bred with Eef1a-LSLL-EGFPL10 TG (hemizygotes) mice to produce double TG animals. Animals were group-housed 2-5 per cage under a 12 hours light/dark cycle (7 am to 7 pm) with a standard diet (Labdiet™, USA) and water *ad libitum*. We began all of the animal experiments using age (8-15 weeks)- and gender (male)-matched littermates. All experimental procedures were approved by the Animal Care and Use Committee of the Daegu Gyeongbuk Institute of Science & Technology (DGIST, IACUC #20011503-03).

Dual fluorescence labeling of dMCs and vMCs

The following AAV stocks to express a fluorescence protein in Cre-dependent manner were used for our experiments: AAV1.CAG.FLEX.EGFP (PENN vector core), and AAV2.CAG.FLEX.tdTomato (UNC vector core). Calcr1-Cre TG mice were deeply anesthetized with an intraperitoneal (i.p.) injection of Avertin (250 mg/kg) and placed into a stereotaxic apparatus (Angle Two™, Leica Biosystems, USA). Original AAV stocks were diluted in 1×10^{12} GC/ml with AAV dilution solution (5% sorbitol in 1X PBS) and 500 nl were injected into either the dorsal hilus (dHil) (-2.1 mm AP, +/-1.4 mm ML, -1.95 mm DV) or ventral hilus (vHil) (-3.3 mm AP, +/-2.7 mm ML, -3.6 mm DV). Flow rate (200 nl/min) was controlled using a Nanopump controller (World Precision Instruments, Florida, USA). The needle was left in the target region after injection for another 5 min. Calcr1-Cre TG mice were allowed at least 3 weeks of rest before the next experimental stage. Any mice with abnormal recovery after stereotaxic surgery were euthanized and thus excluded from the analysis. All injections were verified histologically at the end of the experiments.

Immunohistochemistry and cell counting

All mice were anesthetized by i.p. injection of Avertin (250 mg/kg) and perfused transcardially with PBS, followed by 4% paraformaldehyde (PFA). The brains were extracted and incubated in 4% PFA overnight at 4 °C, before being transferred to 15% sucrose until they sank and then transferred to 30% sucrose

overnight at 4 °C. Brains were coronally or horizontally cut into 40 µm sections using a Cryostat (CM3050S, Leica Biosystems, USA). For immunostaining, each slice was incubated with the blocking buffer (1 X PBS, 0.2% BSA, 4% normal goat serum, 0.3% Triton X-100) at room temperature for 1 hour. After blocking, sections were incubated overnight at 4 °C with primary antibodies diluted in the blocking buffer. Primary antibodies for staining were as follows: anti-GluR2/3 (rabbit polyclonal, 1:100; catalog no. ab1506, Millipore, Germany), anti-calretinin (rabbit polyclonal, 1:500; catalog no. 7699/3h, SWANT, Switzerland), anti-parvalbumin (rabbit polyclonal, 1:1000; catalog no. pv27, SWANT, Switzerland), anti-neuropeptide Y (rabbit polyclonal, 1:1000; catalog no. h-049-03, Phoenix Pharmaceutical, USA), and anti-c-Fos (rabbit polyclonal, 1:1000; catalog no. 2250, Cell Signaling, USA). After incubation for 24 hours, sections were washed three times with washing buffer (1 X PBS, 0.3% Triton X-100) for 10 min, before they were incubated with tyramide signal amplification reagent (catalog no. B40955, ThermoFisher, USA) for GluR2/3 and c-Fos and Alexa-fluor-conjugated secondary antibodies (1:400; Life Technologies, USA) for calretinin, PV, and NPY at room temperature for 3 hours. The sections were washed three times, counterstained with DAPI, and then mounted using Prolong™ Gold (catalog no. P36930, ThermoFisher) anti-fading mounting medium. To determine cell-type specificity in Calcrl-Cre mice, AAV2.CAG.FLEX.tdTomato was injected into either the dHil or vHil, as described above. Sections were coronally prepared and each representative dorsal and ventral region of the sections stained with cell-type markers (GluR2/3, CRT, PV, and NPY) under standard protocol. Images were taken using a confocal microscope (LSM 780, Zeiss, Oberkochen, Germany). Fluorescence labeled neurons with marker in the hilus were manually quantified using ImageJ (NIH, Maryland, USA).

Fluorescence imaging of dMCs and vMCs

Brains were prepared for immunohistochemistry and fluorescence imaging, as described above. Sections were scanned with a confocal microscope (LSM 780/800, Zeiss, Oberkochen, Germany) under the same imaging conditions. The fluorescent intensity was quantified using ImageJ (NIH, Maryland, USA). The average of fluorescent intensity was measured for the region of interest for each hippocampal subregion, including the hilus, the inner molecular layer (IML), the granule cell layer (GCL), the middle molecular layer (MML), and the outer molecular layer (OML). The linescans were 28 µm (40 pixels) wide.

Three-dimensional imaging of MC projections

Clearing of the intact brain: For imaging of the whole hippocampal region, the posterior two-third of a whole postmortem mouse brain was dissected and polymerized in a 1x PBS solution containing 1% acrylamide (acrylamide:bis-acrylamide=29:1) and 0.1% Azo-initiator (VA-044, Wako) overnight, followed by polymerization for 3 hours at 37 °C (X-Clarity polymerization system, Logos Biosystems, South Korea). Polymerized tissues were cleared in an X-Clarity™ tissue clearing system II (Logos Biosystems, South Korea) for 8 hours at a current of 2A, temperature of 37.0 °C, and pump speed of 80 rpm. Cleared tissues were stored in a refractive index matching solution (50% sucrose, 20% urea) for imaging with light-sheet fluorescence microscopy.

Three-dimensional (3D) fluorescence imaging: For light-sheet fluorescence microscopy, we used the Ultramicroscope II from LaVision BioTec (Bielefeld, Germany) equipped with Olympus (Tokyo, Japan) MVPLAPO 0.63x lens with dipping cap, NKT Photonics (Birkerød, Denmark) SuperK EXTREME EXW-12 white light laser, Andor Neo sCMOS camera (Thorlabs, New Jersey, USA) and a customized sample holder. Scans were made at 0.63 magnification with a light sheet numerical aperture adjusted at 0.073. For EGFP and tdTomato fluorescence proteins, excitation filters of 470/40, 560/25 and emission filters of 525/50, 620/60 were used. The scan step-size was set at 3 μm and both channels were obtained in two separate scans. For the image post-processing and 3D image rendering, serial tif image files were converted to an Imaris file format and analyzed with Imaris software (Bitplane, Cologne, Germany).

Quantification of dMCs and vMCs subpopulation

For counting the number of MCs, marker (GluR2/3 and CRT) stained cells were counted on every three sections of the dorsal (#1 ~ #3) and twelve sections of the ventral (#4 ~ #8) DG along the longitudinal axis of the hippocampus. The horizontal shape of the DG from the dorsal to the medial part varies greatly, while the ventral part is nearly uniform. To quantitatively analyze a total of dMCs and vMCs in each mouse, MC subpopulations were calculated as: 3 times the number of dMCs (GluR2/3|+CRT-) in each dorsal section (#1 ~ #3) and 12 times the number of vMCs (GluR2/3|+CRT+) in each ventral section (#4 ~ #8).

Transcriptional profiling of dMCs and vMCs

Sample preparation and TRAP: TRAP assay was conducted with minor modification of the original procedure⁴⁰, as described below. Drd2-Cre female mice (hemizygote) were cross-bred with Eef1a-LSL-EGFP10 male mice to produce MC-TRAP (Drd2-Cre;Eef1a¹LSL.eGFPL10a/+) mice. MC-TRAP male mice around 10 weeks old were used for MC transcriptome analysis. After decapitation, the brains were rapidly soaked in the pre-chilled dissection buffer (1 x HBSS, 2.5 mM HEPES [pH 7.4], 35 mM glucose, 4 mM NaHCO₃, 100 $\mu\text{g}/\text{ml}$ cycloheximide, RNase-free Water) for 1 min. The hippocampi of 25 MC-TRAP mice were quickly manually dissected and separated into the dorsal and ventral parts. Five mice per group were pooled for each TRAP to achieve the necessary minimum yield for RNA sequencing. Pooled hippocampal tissues were kept under dissection buffer for 30 min to minimize blood trace and then homogenized in ice-cold polysome extraction buffer (20 mM HEPES [pH 7.4], 150 mM KCl, 10 mM MgCl₂, 0.5 mM dithiothreitol, 100 $\mu\text{g}/\text{ml}$ cycloheximide, protease inhibitors [EDTA-free], 400 unit/ml recombinant RNase inhibitors, and 200 unit/ml Superasin) with a motor-driven Teflon glass homogenizer. Homogenates were cleared by centrifugation at 2000 x g for 10 min at 4 °C. NP-40 (EMD Biosciences, California, USA) and 1,2-diheptanoyl-sn-glycero-3-phosphocholine (DHPC; Avanti Polar Lipids, Alabama, USA) were added to the supernatant at a final concentration of 1% and 30 mM, respectively, followed by incubation on ice for 5 min. The clarified lysates were centrifuged for 10 min at 20,000 g to pellet insolubilized materials. Monoclonal anti-EGFP antibodies (50 μg each of the clones 19C8 and 19F7) were immobilized onto Dyna magnetic beads (Invitrogen, California, USA) via protein L. These EGFP-affinity beads were added to the supernatant, followed by incubation using an end-over-end rotator for 16 hours

at 4 °C. Polysome-bound beads were washed 3 times in the high-salt washing buffer (20 mM HEPES [pH 7.4], 350 mM KCl, 5 mM MgCl₂, 1% NP-40, 0.5 mM dithiothreitol, 100 µg/ml cycloheximide, and RNase-free water) with gentle agitation to resuspend the beads between washing steps. The beads were washed one more time with detergent-free washing buffer and immediately added to RLT buffer, followed by RNA purification with RNeasy Micro Kit (QIAGEN, California, USA) with in-column DNase digestion. The quantity and integrity of purified RNA was determined by using a Quant-iT RiboGreen RNA Assay Kit (ThermoFisher, Massachusetts, USA) and Fragment analyzer (AATI, USA), and only samples with RNA Quality Number (RQN) greater than eight (out of ten) were used for qPCR and RNA-seq.

qPCR analysis: The isolated RNA from the TRAP assay was used to synthesize cDNA with iScript cDNA Synthesis Kit (BioRad, California, USA). 10 ng of cDNA was used for each Quantitative real-time PCR (qPCR) reaction and all samples were run in triplicate. qPCR analysis was carried out using SsoAdvance Universal SYBR Green Supermix (BioRad, California, USA) and AriaMx Real-Time PCR system (Agilent, Technologies, California, USA) following standard cycling conditions (95 °C for 30 s, then 40 cycles of 95 °C for 5 s and then 60 °C for 30 s). The relative quantitation of mRNA was calculated by the comparative Ct method after normalization to mouse Map2. The following primers were used: Calb2, 5'-TTTATGGAGGCTTGGCGGAA-3' (forward) and 5'-TCATCATAGGGCCTGTTGGC-3' (reverse); Gria3, 5'-CTCCAAGGACAAGACCAAGTGC-3' (forward) and 5'-GTTTGGACTCTGCCCGTGAT-3' (reverse). Non-specific amplification was excluded by confirming single melting curve patterns and ethidium bromide staining on 2% agarose gels. All statistical analyses were using Student's t test.

Data analysis: Full-length cDNA was generated from 500 pg of RNA with Ovation RNAseq V2 kit (NuGene, California, USA). cDNA quality and quantity had been checked on a Fragment Analyzer using DNA High sensitivity assay kit (AATI, USA) prior to sequencing library preparation. Sequencing libraries were constructed by a TruSeq RNA library Prep Kit v2 (Illumina, California, USA) and sequenced for 50 bp paired-end on Illumina HiSeq2500 using Rapid V2 sequencing chemistry (Illumina, California, USA). For each library, the number of detected genes is presented in Table S1. Reads were then aligned to the mouse reference genome (GRCm38) using STAR version 2.5.2b. Read counts per gene were calculated using HTseq-count version 0.7.2. Differential expression analysis on raw read counts was performed in R using the edgeR package. The package implements exact statistical methods based on generalized linear models. The particular feature of edgeR functionality is empirical Bayes methods that permit the estimation of gene-specific biological variation, even for experiments with minimal levels of biological replication. The quasi-likelihood method is implemented for differential expression analyses of bulk RNA-seq data. We first identified 'expressed' genes as the genes with counts per million fragments mapped (CPM) larger than 1 under at least two of the biological replicates. Finally, we identified DEGs as the ones that have the adjusted p values < 0.05 and absolute log₂-fold-changes > 0.58 (1.5-fold). GO and KEGG pathway analysis were performed in DAVID software using Fisher's exact test.

Gi-DREADD-dependent MC manipulation

The AAV8.hSyn.DIO.hM4Di-mCherry (PENN vector core) virus was injected in either the dHil or vHil as described above. Control animals were injected with AAV8.hSyn.DIO.mCherry. All MC-specific and region-specific expression of all injections were verified histologically at the end of experiments. The back-metabolized clozapine from CNO may lead to activation of endogenous receptors in non-DREADD animals, thus we applied low-dose CNO (less than 1 mg kg^{-1}) to avoid potential side effects in a higher dose (10 mg kg^{-1}) for our behavioral testing. CNO (Sigma-Aldrich, Missouri, USA) in 0.9% saline was injected i.p. as indicated in Fig. 4 and Fig. 5.

c-Fos Immunohistochemistry in GCs and PV+BCs

For counting c-Fos positive neurons in the DG, mice received CNO (1.0 mg kg^{-1}) i.p 30 min before contextual fear conditioning. Then, mice explored the conditioning chamber with a foot shock. After this, mice returned to their home cage in either 90 min or 30 min to examine GCs and PV+BCs activity, respectively. Brains were sectioned coronally and horizontally from each animal. The outline of GCL and SGZ for quantification of GCs and PV+BCs were manually drawn by well-defined anatomical landmarks visualized with staining DAPI. The number of c-Fos positive GCs and PV+BCs were counted on three and two representative dorsal and ventral sections, respectively. The density of neurons in the DG was calculated dividing the number of cells by the total area.

Anxiety-related behavioral testing

All experiments were conducted during the light cycle (7 am to 7 pm). Mice were handled for 1 min on three consecutive days before testing and were randomly assigned to a blinded investigator. Mice were administrated CNO i.p. 120 min before the test was conducted

Elevated plus maze test: the elevated plus maze consisted of two open arms and two enclosed arms ($30 \times 5 \text{ cm}$) with a center platform ($5 \times 5 \text{ cm}$). The entire apparatus was placed 50 cm above the floor. Mice were habituated in the testing room in their home cages for 60 min before the test was conducted. Each mouse was placed in the center platform and facing the enclosed arm. The time spent in the open arm was measured using an automated video-tracking system (EthoVision XT, Noldus, USA) for 5 min. Between sessions, the apparatus was cleaned using 70% ethanol.

Open field test: locomotor activity was measured in an open-field area ($40 \times 40 \times 40 \text{ cm}$) using EthoVision XT for 30 min. Mice were transferred to the testing room and acclimated for 1 hour before the test. The center zone index was defined as the center travel distance ($20 \times 20 \times 20 \text{ cm}$) versus total travel distance. After every session, the open field was cleaned with 70% ethanol.

Contextual fear conditioning

The chamber for Context A (paired with shock) was a $15 \times 15 \times 20 \text{ cm}$ chamber with a metal grid, white lighting, and background noise (provided by a fan) that was covered by a transparent acrylic lid. For context B (with no shock), the chamber had a checkered cylindrical wall, grid pattern, no background

noise, and the odor of 0.25% benzaldehyde (in 100% ethanol) provided using a paper dipped in the solution and placed beneath the chamber during experiments. All mice were acclimated in the anteroom for 1 hour before the test. Mice were allowed to train the context for 180 sec and then received a foot shock (2 sec, 0.5 mA), followed by a post-shock period of 60 sec. Freezing scores were measured using Freezeframe 4 (Actimetrics Software, Evanston, IL, USA). The threshold was set at 20, and the freezing bout was set at 1 sec. The chamber and grid were cleaned with 70% ethanol between sessions.

Memory encoding test: mice were administrated CNO i.p. 120 min before training context. Mice were placed in context A, followed by a foot shock and a 60 sec post-shock period. After training, mice were returned to their home cage. 24 hours later, mice explored in the shock-associated context again to recall fear memory for 4 min. Freezing scores were quantified for 3 min using Freezeframe 4 (Actimetrics Software, Evanston, IL, USA).

Contextual discrimination: this procedure was based on a protocol described in detail previously³⁴. For contextual fear acquisition, mice were trained in context A to associate fear memory for consecutive 3 days (days 1-3). Mice were allowed to explore context A for 180 sec, were administered a foot shock (2 sec, 0.5 mA), and were then returned to cage 60 sec later. For contextual generalization, mice were placed in context A or context B without shock for 240 sec and then were placed in the opposite context for 240 sec 1.5–2 hours later (counterbalanced order) on consecutive 2 days (days 4-5). For contextual discrimination training, mice were administrated CNO i.p. 120 min before discrimination of contexts. They were placed in context B (not paired with shock) for 240 sec. following 1.5-2 hours context B, they were placed in context A (again paired with shock) for 180 sec, received a 2 sec 0.5 mA shock, left in the chamber for 60 sec following the shock. Mice were trained to discriminate in both contexts on each day for 12 days. The alternative training orders followed a BAAB → ABBA pattern (day 6, B → A; day 7 A → B, day 8, A → B; day 9, B → A; day 10, A → B; day 11, B → A; day 12, B → A; day 13, A → B; days 6 through 17). Freezing scores were measured for an initial explored time of 180 sec. For contextual discrimination presentation, the freezing score was combined consecutive 2 days into the block, so that each block consisted of a freezing score of consecutive 2 days in both context A and B. The inhibition of each MC subpopulation and their control group was alternatively performed.

Data analysis and statistics

All data are represented as mean ± standard error of the mean (SEM). Statistical parameters and analysis performed can be found in the figure legends and Supplementary Table 3. Statistical analyses were performed using Prism 7.0a (GraphPad, La Jolla, CA). A comparison of two groups was analyzed by Student's t-test (paired and unpaired, two-tailed). Two-way ANOVA or repeated measures ANOVA for more than two groups were used to investigate main effects and Bonferroni-corrected post hoc comparisons.

Declarations

Acknowledgements

We are grateful to Dr. Jia Chang (The Rockefeller University, USA) for helpful advice and discussion and also to Dr. Kazu Nakazawa (University of Alabama, USA) for kindly sharing Calcr1-Cre transgenic mice. This research was supported by the Brain Research Program through the National Research Foundation of Korea (NRF) funded by the Ministry of Science, ICT (NRF2017M3C7A1048448 to YSO); the Basic Science Research Program through the National Research Foundation of Korea (NRF) funded by the Ministry of Education (NRF2020R1F1A1076871 to YSO); KBRI basic research program through Korea Brain Research Institute funded by Ministry of Science and ICT (20-BR-04-03 to YSO); The Basic Science Research Program through the National Research Foundation of Korea(NRF) funded by the Ministry of Education (NRF2019R1I1A1A01063000 to JHJ); The Basic Science Research Program through the National Research Foundation of Korea (NRF) funded by the Ministry of Education (NRF2020R1F1A107687111 to MSJ).

Author contributions

MSJ, JHJ, PG, and YSO designed experiments and conceptualized and performed analyses. MSJ and OSJ performed and analyzed animal surgery, virus injections, histology, and behavioral experiments. MSJ, YC, YSC, and CMH performed and analyzed CLARTY imaging acquisition and processing. JHJ and MSJ performed and analyzed cell-type specific RNA-seq, data analysis, and graphical illustration. YSO supervised the entire work.

Competing interests

The authors declare that they have no competing interests.

Data and materials availability

All data needed to evaluate the conclusions in the paper are present in the paper and/or the Supplementary Materials. Additional data are available from authors upon request.

References

1. Nestler, E.J. et al. Neurobiology of Depression. *Neuron* **34**, 13–25 (2002).
2. Maren, S., Phan, K.L. & Liberzon, I. The contextual brain: implications for fear conditioning, extinction and psychopathology. *Nature Reviews Neuroscience* **14**, 417–428 (2013).
3. Strange, B.A., Witter, M.P., Lein, E.S. & Moser, E.I. Functional organization of the hippocampal longitudinal axis. *Nature Reviews Neuroscience* **15**, 655 (2014).
4. Bannerman, D.M. et al. Hippocampal synaptic plasticity, spatial memory and anxiety. *Nature Reviews Neuroscience* **15**, 181–192 (2014).
5. Kheirbek, Mazen A. et al. Differential Control of Learning and Anxiety along the Dorsoventral Axis of the Dentate Gyrus. *Neuron* **77**, 955–968 (2013).

6. Cembrowski, M.S. & Spruston, N. Heterogeneity within classical cell types is the rule: lessons from hippocampal pyramidal neurons. *Nature Reviews Neuroscience* **20**, 193–204 (2019).
7. Scharfman, H.E. The enigmatic mossy cell of the dentate gyrus. *Nature Reviews Neuroscience* **17**, 562 (2016).
8. Jinde, S. et al. Hilar Mossy Cell Degeneration Causes Transient Dentate Granule Cell Hyperexcitability and Impaired Pattern Separation. *Neuron* **76**, 1189–1200 (2012).
9. Bui, A.D. et al. Dentate gyrus mossy cells control spontaneous convulsive seizures and spatial memory. *Science* **359**, 787–790 (2018).
10. Oh, S.-J. et al. Hippocampal mossy cell involvement in behavioral and neurogenic responses to chronic antidepressant treatment. *Molecular Psychiatry* (2019).
11. Amaral, D.G., Scharfman, H.E. & Lavenex, P. The dentate gyrus: fundamental neuroanatomical organization (dentate gyrus for dummies). *Prog Brain Res* **163**, 3–22 (2007).
12. Buckmaster, P.S., Wenzel, H.J., Kunkel, D.D. & Schwartzkroin, P.A. Axon arbors and synaptic connections of hippocampal mossy cells in the rat in vivo. *Journal of Comparative Neurology* **366**, 270–292 (1996).
13. Ratzliff, A.d.H., Howard, A.L., Santhakumar, V., Osapay, I. & Soltesz, I. Rapid Deletion of Mossy Cells Does Not Result in a Hyperexcitable Dentate Gyrus: Implications for Epileptogenesis. *The Journal of Neuroscience* **24**, 2259–2269 (2004).
14. Botterill, J.J. et al. An Excitatory and Epileptogenic Effect of Dentate Gyrus Mossy Cells in a Mouse Model of Epilepsy. *Cell Reports* **29**, 2875–2889.e2876 (2019).
15. Hsu, T.-T., Lee, C.-T., Tai, M.-H. & Lien, C.-C. Differential Recruitment of Dentate Gyrus Interneuron Types by Commissural Versus Perforant Pathways. *Cerebral Cortex* **26**, 2715–2727 (2015).
16. Yeh, C.-Y. et al. Mossy Cells Control Adult Neural Stem Cell Quiescence and Maintenance through a Dynamic Balance between Direct and Indirect Pathways. *Neuron* **99**, 493–510.e494 (2018).
17. Fredes, F. et al. Novelty gates memory formation through ventro-dorsal hippocampal interaction. *bioRxiv*, 673871 (2019).
18. Blasco-Ibáñez, J.M. & Freund, T.F. Distribution, ultrastructure, and connectivity of calretinin-immunoreactive mossy cells of the mouse dentate gyrus. *Hippocampus* **7**, 307–320 (1997).
19. Espinoza, C., Guzman, S.J., Zhang, X. & Jonas, P. Parvalbumin + interneurons obey unique connectivity rules and establish a powerful lateral-inhibition microcircuit in dentate gyrus. *Nature Communications* **9**, 4605 (2018).
20. Hu, H., Gan, J. & Jonas, P. Fast-spiking, parvalbumin ⁺ GABAergic interneurons: From cellular design to microcircuit function. *Science* **345**, 1255263 (2014).
21. Förster, E., Zhao, S. & Frotscher, M. Laminating the hippocampus. *Nature Reviews Neuroscience* **7**, 259–268 (2006).
22. Stein, E. et al. A Role for the Eph Ligand Ephrin-A3 in Entorhino-Hippocampal Axon Targeting. *The Journal of Neuroscience* **19**, 8885–8893 (1999).

23. Williams, S.E. et al. Ephrin-B2 and EphB1 Mediate Retinal Axon Divergence at the Optic Chiasm. *Neuron* **39**, 919–935 (2003).
24. Sloviter, R.S. Permanently altered hippocampal structure, excitability, and inhibition after experimental status epilepticus in the rat: The “dormant basket cell” hypothesis and its possible relevance to temporal lobe epilepsy. *Hippocampus* **1**, 41–66 (1991).
25. Nörenberg, A., Hu, H., Vida, I., Bartos, M. & Jonas, P. Distinct nonuniform cable properties optimize rapid and efficient activation of fast-spiking GABAergic interneurons. *Proceedings of the National Academy of Sciences* **107**, 894–899 (2010).
26. Südhof, T.C. Towards an Understanding of Synapse Formation. *Neuron* **100**, 276–293 (2018).
27. Beuter, S. et al. Receptor tyrosine kinase EphA7 is required for interneuron connectivity at specific subcellular compartments of granule cells. *Scientific Reports* **6**, 29710 (2016).
28. Müller, T. et al. Neuregulin 3 promotes excitatory synapse formation on hippocampal interneurons. *The EMBO Journal* **37**, e98858 (2018).
29. Hainmueller, T. & Bartos, M. Dentate gyrus circuits for encoding, retrieval and discrimination of episodic memories. *Nature Reviews Neuroscience* **21**, 153–168 (2020).
30. Anacker, C. et al. Hippocampal neurogenesis confers stress resilience by inhibiting the ventral dentate gyrus. *Nature* **559**, 98–102 (2018).
31. Medrihan, L. et al. Reduced Kv3.1 Activity in Dentate Gyrus Parvalbumin Cells Induces Vulnerability to Depression. *Biological Psychiatry* (2020).
32. Zou, D. et al. DREADD in parvalbumin interneurons of the dentate gyrus modulates anxiety, social interaction and memory extinction. *Curr Mol Med* **16**, 91–102 (2016).
33. McHugh, T.J. et al. Dentate Gyrus NMDA Receptors Mediate Rapid Pattern Separation in the Hippocampal Network. *Science* **317**, 94–99 (2007).
34. Nakashiba, T. et al. Young Dentate Granule Cells Mediate Pattern Separation, whereas Old Granule Cells Facilitate Pattern Completion. *Cell* **149**, 188–201 (2012).
35. Danielson, N.B. et al. In Vivo Imaging of Dentate Gyrus Mossy Cells in Behaving Mice. *Neuron* **93**, 552–559.e554 (2017).
36. Czerniawski, J., Ree, F., Chia, C. & Otto, T. Dorsal versus ventral hippocampal contributions to trace and contextual conditioning: Differential effects of regionally selective nmda receptor antagonism on acquisition and expression. *Hippocampus* **22**, 1528–1539 (2012).
37. Maren, S. & Holt, W.G. Hippocampus and Pavlovian Fear Conditioning in Rats: Muscimol Infusions Into the Ventral, but Not Dorsal, Hippocampus Impair the Acquisition of Conditional Freezing to an Auditory Conditional Stimulus. *Behavioral Neuroscience* **118**, 97–110 (2004).
38. Huckleberry, K.A. et al. Dorsal and ventral hippocampal adult-born neurons contribute to context fear memory. *Neuropsychopharmacology* **43**, 2487–2496 (2018).
39. Weeden, C.S.S., Hu, N.J., Ho, L.U.N. & Kesner, R.P. The role of the ventral dentate gyrus in olfactory pattern separation. *Hippocampus* **24**, 553–559 (2014).

Figures

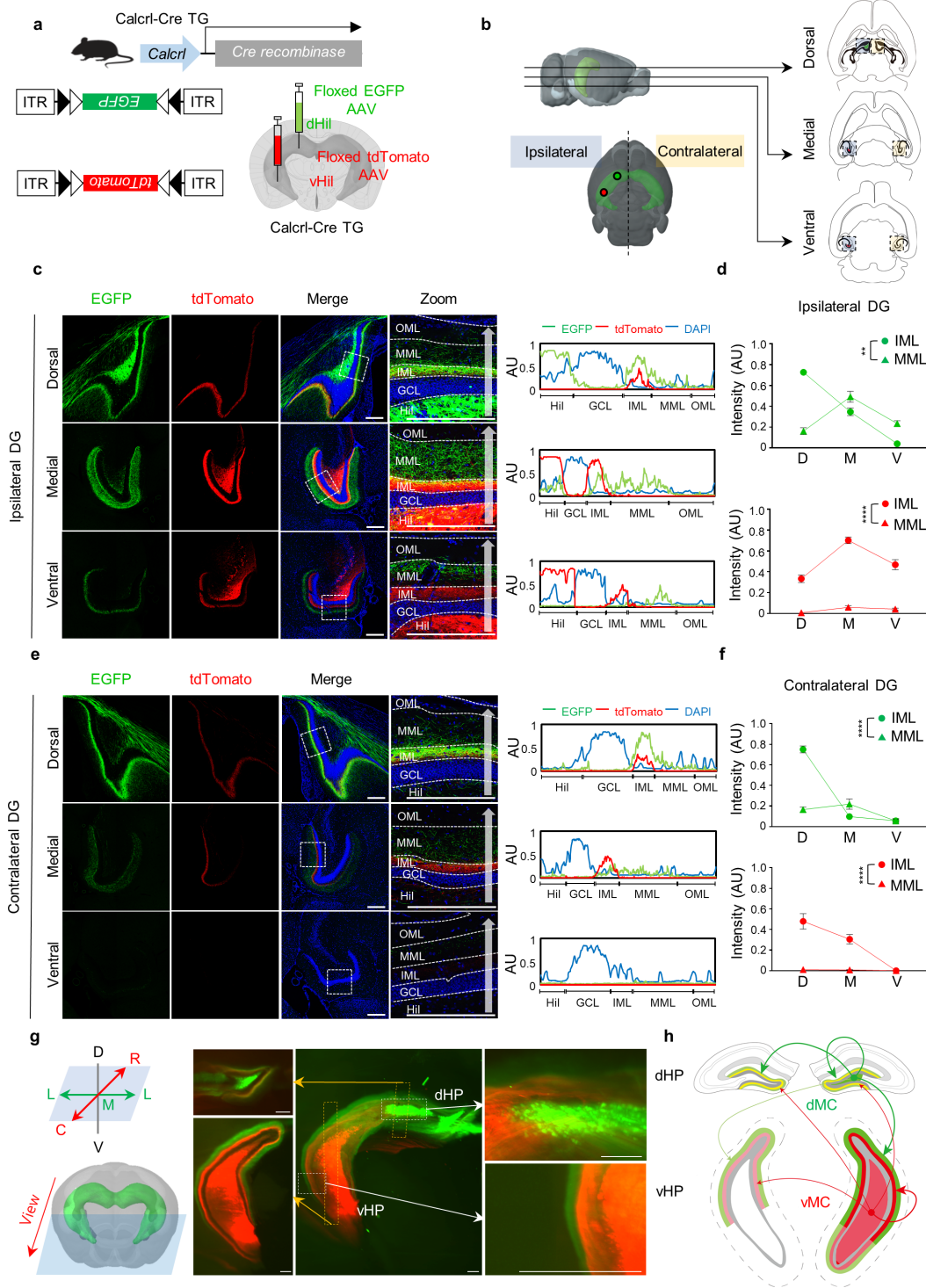


Fig. 1

Figure 1

dMCs and vMCs extend distinct axonal projections along the longitudinal axis of the DG. a Representative viral injections in either the dorsal hilus (dHil) or ventral hilus (vHil) of Calcrl-Cre mice. See also Supplementary Figure 1 for cell-type specificity. b Schematics depicting fluorescence imaging of the DG along the DV axis. c-f Representative fluorescence of the ipsilateral (c, d) and contralateral (e, f) DG images showing axonal projections of dMCs (EGFP) and vMCs (tdTomato) along the DV axis. Fluorescence intensity of each channel (area unit) was normalized to a maximum value of 1. Hil, hilus; GCL, granule cell layer; IML, inner molecular layer; MML, middle molecular layer; OML, outer molecular layer. Scale bar, 200 μm . g Three-dimensional rendering of sequential hippocampal images. dHP, dorsal hippocampus commissural fiber; vHP, ventral hippocampus. Scale bar, 300 μm . h Schematic illustration of connectivity between dMCs (green) and vMCs (red) along the DV axis of the DG.

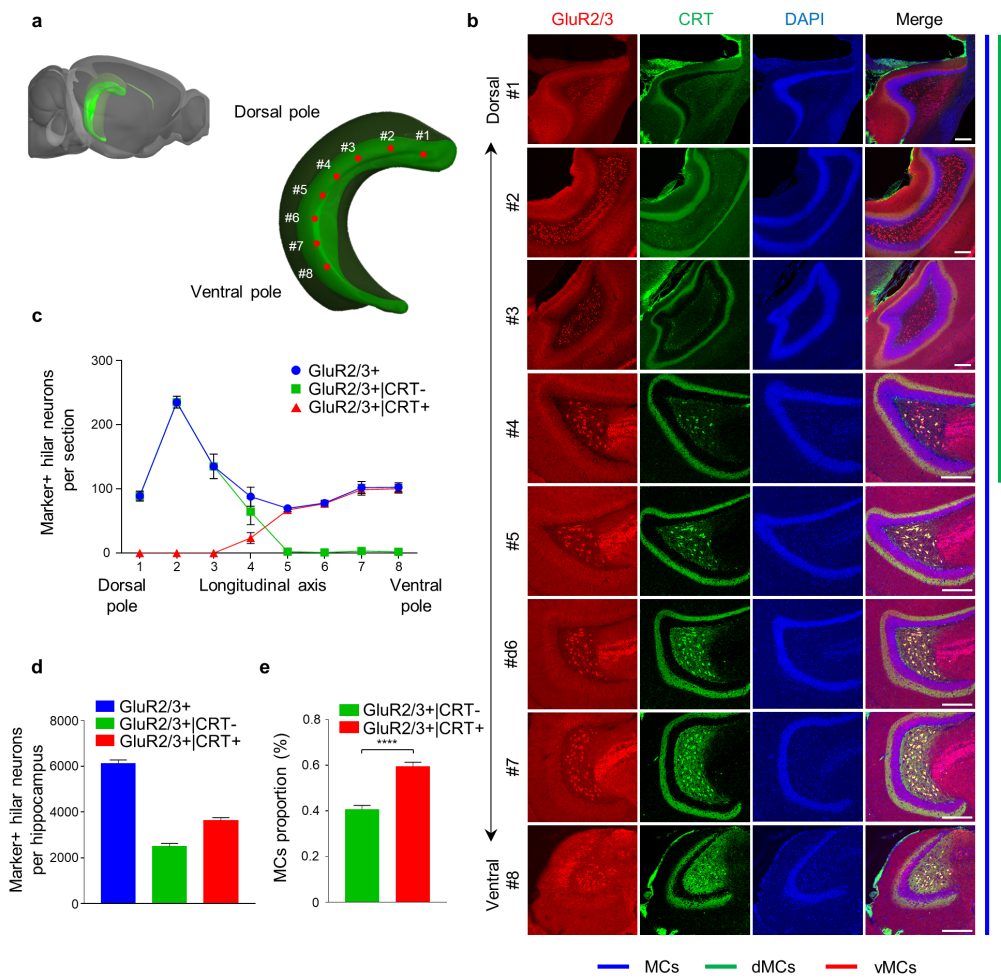


Fig. 2

Figure 2

Two distinct MC subpopulations are spatially segregated along the DV axis. a Schematics depicting histological analysis of the DG along the DV axis. b Representative images showing GluR2/3 (red, pan MCs marker) and CRT (green, ventral MCs marker) expressions along the DV axis. Scale bar, 200 μ m. c Distribution of each MC subpopulation along the DV axis of the DG. The markers are indicated in GluR2/3+|CRT- as dMCs and GluR2/3+|CRT+ as vMCs. d Cell number of each MC subpopulation per

hippocampus. e Ratio of each MC subpopulation versus total MCs (****p < 0.0001, paired t test). All data represented as mean ± SEM.

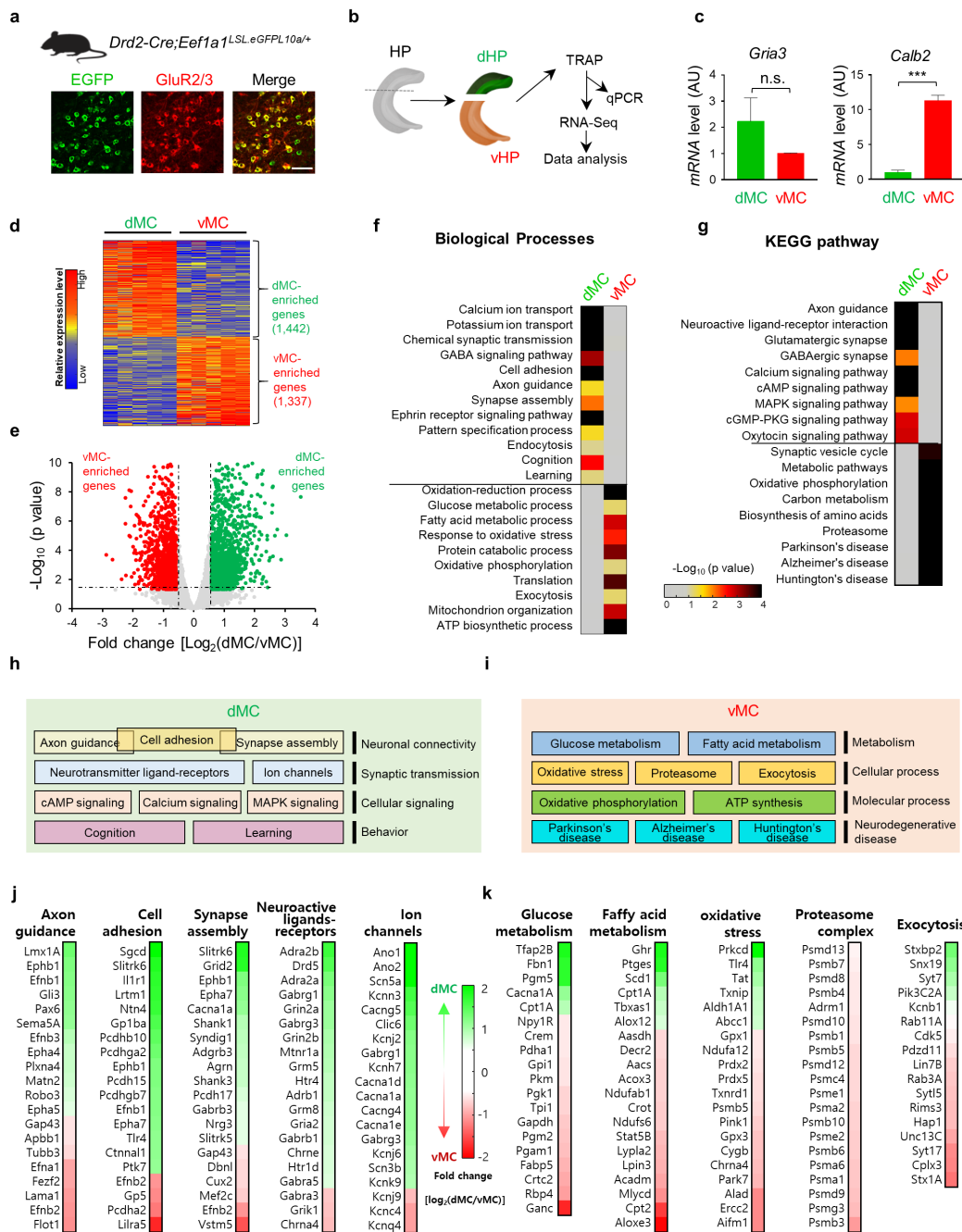


Fig. 3

Figure 3

Transcriptional heterogeneity between dMCs and vMCs are associated with distinct neuronal properties. a EGFP/10a expressions in GluR2/3+ MCs. Scale bar, 50 μm. b Experimental schematics for DV segmentation of the hippocampus and subsequent TRAP RNA-sequencing. c Quantitative PCR data

showing Gria3 and Calb2 expressions in either dMC- or vMC fraction (n = 5 per each groups, ***p < 0.001, unpaired t test). d Heatmap showing DEGs of dMCs and vMCs. Enriched or de-enriched genes in each fraction are indicated in red and green, respectively. A total number of enriched genes are given in brackets. e Volcano plot showing DEGs of dMCs and vMCs. Genes enriched in each subpopulation plotted in green or red dots, as indicated. Dash line indicate cutoff: fold difference > 1.5, p < 0.05, quasi-likelihood test. f, g Functional enrichment analysis with DEGs in annotated functional categories: Gene Ontology biological process (f) and KEGG pathway (g) (p < 0.05, fisher's exact test). h, i Graphical representations of dMC- (h) or vMC-enriched (i) gene families with 4 layers of functional categories that organize neuronal properties. j, k Heatmaps showing the top 20 DEGs exhibiting the highest fold difference between dMCs (j) and vMCs (k) in each functional category.

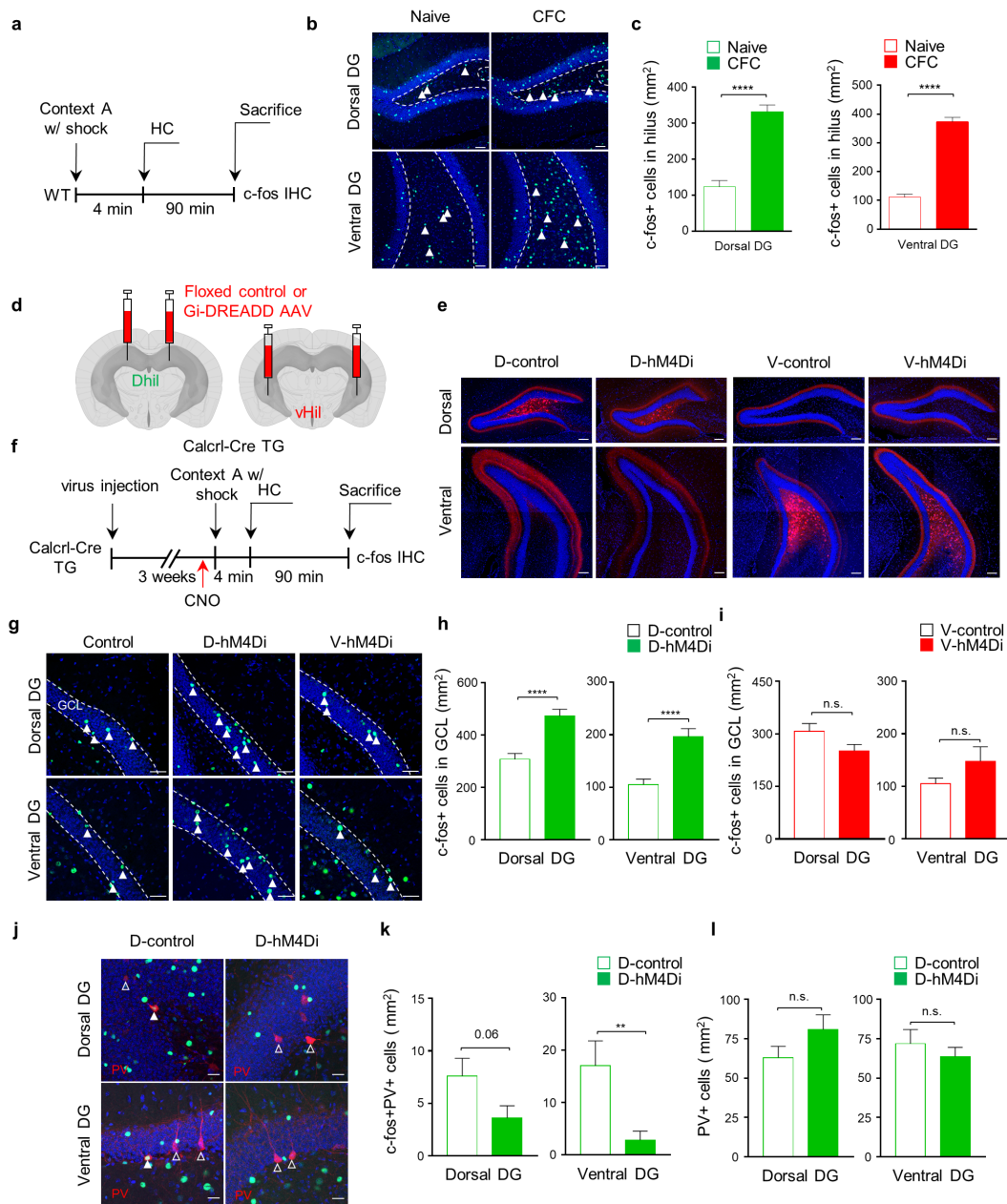


Fig. 4

Figure 4

Acute inhibition of dMCs, but not of vMCs, results in hyperexcitation of GCs across the DV axis of the DG. a Schematics for experimental design for histological measurement of MC activation along the DV axis, in response to contextual stimuli. HC, homecage. b Representative images showing c-Fos immunoreactivity along the DV axis. Arrowheads indicate c-Fos+ cells in the hilus. CFC, contextual fear conditioning. Scale bar, 50 μ m. c The number of c-Fos+ cells in the dHil or the vHil. A total number of c-

Fos+ cells were normalized with the hilar area (mm²) (****p < 0.0001, t test). d Representative viral injections of floxed control and Gi-DREADD in either the dHil or the vHil. e Representative images showing dMC- and vMC-specific expressions of mCherry (D- and V-control) or Gi-DREADD (D- and V-hM4Di). Scale bar, 100 μm. f Schematics for experimental design for histological measurement of GC activation under chemogenetic inhibition of either dMCs or vMCs. g Representative images showing c-Fos immunoreactivity of GCs in the dorsal and ventral DG of Gi-DREADD groups in comparison with control. h, I The number of c-Fos+ GCs in the dorsal and ventral DG, as indicated (D- and V-control n = 5, D-hM4Di n = 5, V-hM4Di n = 3, 3 slices per mice, ****p < 0.0001, unpaired t test). j Representative images showing c-Fos immunoreactivity in PV+BCs in the dorsal and ventral DG. Scale bar, 20 μm. k The number of c-Fos+ BCs (PV+) in the dorsal and ventral DG, as indicated (D-control n = 3, D-hM4Di n = 5, 2 slices per mice **p < 0.01, unpaired t test). l The number of PV+ BCs in the dorsal and ventral DG. All data represented as mean ± SEM.

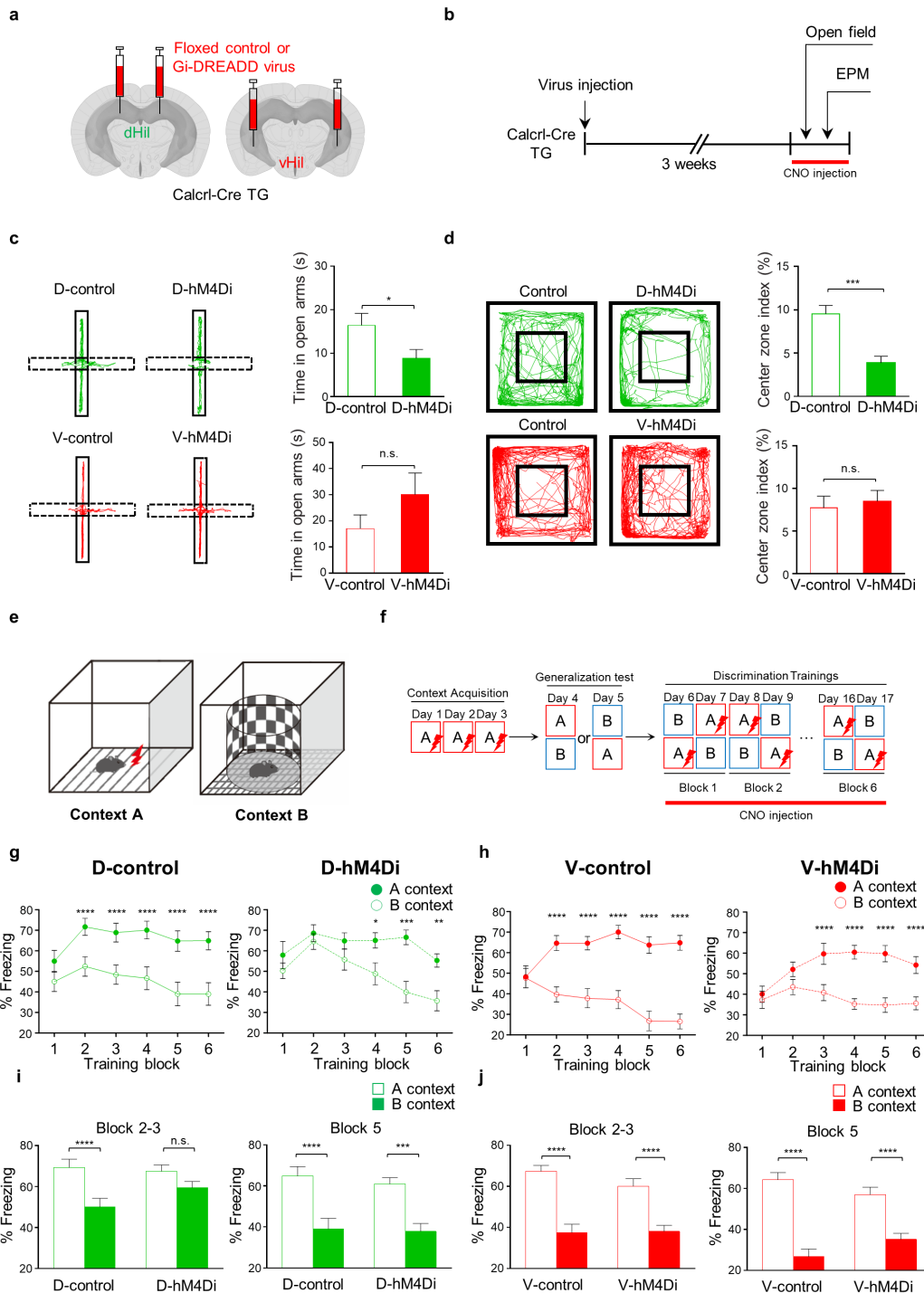


Fig. 5

Figure 5

dMCs are crucial for anxiety control and contextual pattern separation. a Representative viral injections. b Schematics for experimental design to measure behavioral anxiety. c, d Behavioral anxiety of dMC groups (D-control n = 9 and D-hM4Di n = 10) and vMC groups (V-control n = 9 and V-hM4Di n = 10) in the elevated plus maze test (c) and the open field test (d) (*p < 0.05, ***p < 0.001, unpaired t test). e Schematic illustration depicting distinct context A and B. f Schematic experimental paradigm for the

contextual discrimination test. g, h Freezing behavior in context A (filled circles) and B (open circles) of dMC groups (D-control n = 10 and D-hM4Di n = 8) (g) and vMC groups (V-control n = 10 and V-hM4Di n = 9) (h). * indicates Bonferroni's multiple comparison, **p < 0.01, ***p < 0.001, and ****p < 0.0001. i, j Freezing behavior between distinct contexts pair in the block 2-3 and the block 5 of dMCs group (i) and vMCs group (j). Repeated measurement ANOVAs found significant interaction in dMC groups (context x D-hM4Di), p = 0.049. * indicates Bonferroni's multiple comparison, ***p < 0.001, and ****p < 0.0001. All data represented as mean ± SEM.

Supplementary Files

This is a list of supplementary files associated with this preprint. Click to download.

- [SupplementaryFigure.pdf](#)
- [SupplementaryTable1.xlsx](#)
- [SupplementaryTable2.xlsx](#)
- [SupplementaryMovie1.mp4](#)